RESEARCH ARTICLE

Correspondence to:
E. C. Smith,
emit1@bas.ac.uk

Mapping the ice-bed interface characteristics of Rutford Ice Stream, West Antarctica, using microseismicity

E. C. Smith[1,2], A. M. Smith[1], R. S. White[2], A. M. Brisbourne[1], and H. D. Pritchard[1]

[1]British Antarctic Survey, Natural Environment Research Council, Cambridge, UK, [2]Bullard Laboratories, Department of Earth Sciences, University of Cambridge, Cambridge, UK

Abstract Flow dynamics of the ice streams that drain the Antarctic Ice Sheet are heavily influenced by processes at the bed. Natural seismic activity generated beneath an ice stream is associated with the motion of the ice over its bed and can be used to map both the characteristics of the ice-bed interface and to understand these basal processes. Basal microseismicity was recorded over a 34 day period on Rutford Ice Stream, West Antarctica, using 10 three-component geophones 40 km upstream of the grounding line. Around 3000 microseismic events were located in discrete spatial clusters near the ice-bed interface. The activity of each cluster varies with time, and the source mechanism for the events is interpreted as subhorizontal, low-angle faulting, slipping in the ice flow direction. Cluster locations are interpreted as "sticky spots" of stiff basal sediment at the ice-bed interface, where ice movement is accommodated by stick-slip basal sliding. The sticky spots occur in areas where independent active-source seismic surveys show low porosity sediments at the bed. We show that the sticky spots probably accommodate only a small amount of the total basal motion. Our results suggest that most of the ice stream basal motion is accommodated by aseismic deformation of soft, dilatant basal sediment, or by a well-lubricated, stiffer bed.

1. Introduction

Mass discharge from the West Antarctic Ice Sheet (WAIS) is dominated by fast-flowing ice streams, which transport as much as 90% of the mass of the ice sheet [*Bamber et al.*, 2000] into ice shelves and the ocean. Ice stream dynamics are known to be highly dependent on processes that occur at their base, both sliding over a consolidated (nondeforming) bed and deformation of water saturated subglacial till [*Paterson*, 1994]. These processes occur in combination beneath a number of Antarctic ice streams [e.g., *Vaughan et al.*, 2003; *Alley*, 1993]. Determination of the spatial and temporal organization of these processes is fundamental to our ability to predict the evolution of ice streams and thus the future stability of WAIS and its contribution to global sea level rise [*Rignot et al.*, 2011].

Observing the basal environment of ice streams is challenging. Direct observation by drilling is possible [e.g., *Engelhardt et al.*, 1990], but this method is limited by logistical difficulties in drilling in an ice stream environment and only gives an insight into a very specific area of the ice stream bed. Seismic reflection and radio echo sounding (RES) surveys have been used to map the ice-bed interface and to provide details of spatial variation in basal material and hydrology [e.g., *Blankenship et al.*, 1986; *Smith*, 1997b; *Murray et al.*, 2008]. Repeat observations have also been used to infer temporal changes in basal conditions [*Smith et al.*, 2007], showing that subglacial bedforms and properties can evolve over decadal timescales or less. A useful extension to these techniques is monitoring of natural seismic emissions from the base of ice streams [*Blankenship et al.*, 1987] to provide a direct record of the temporal and spatial seismicity associated with ice movement. The technique has been used extensively to infer basal conditions [*Anandakrishnan and Bentley*, 1993; *Ekström et al.*, 2003; *Smith*, 2006; *Wiens et al.*, 2008; *Walter et al.*, 2010; *Winberry et al.*, 2013], track subglacial water movement [*Winberry et al.*, 2009], and infer grounding zone conditions [*Pratt et al.*, 2014]. The exact source of basal seismicity is still an important and unanswered question, which has proven difficult to constrain due to location uncertainty, and it is still not clear whether basal seismicity originates in the ice, at the interface, or in the subglacial material. This paper presents new results from a passive microseismic data set collected on Rutford Ice Stream. We determine the location of basal seismicity and investigate the source and magnitude of uncertainties in this location using synthetic seismic models. This allows better constraints to be placed on the likely origin of these events. The source magnitudes, source mechanisms, and temporal variation of basal seismicity are determined to provide further evidence to support the likely source of these events. We show
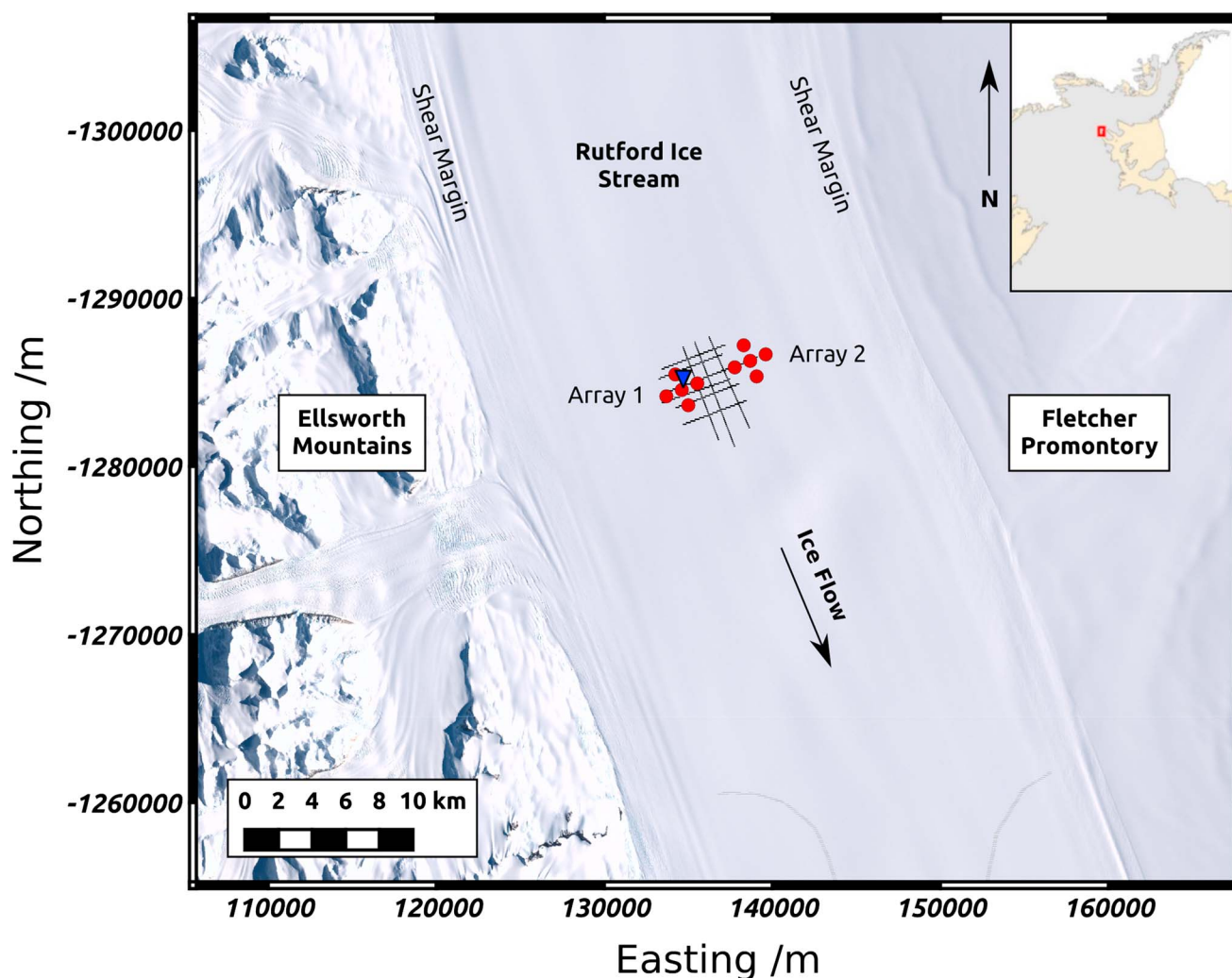
Figure 1. Location of study site on Rutford Ice Stream, background is the Landsat Image Mosaic of Antarctica (LIMA), projection is South Pole Stereographic. Seismic stations (red) are approximately 40 km upstream from the grounding line (grey line—determined by DInSAR data, NASA MeaSURES program). Stations are configured into two cross arrays situated over areas previously identified as having contrasting bed types from active seismic surveying. Seismic lines used to make this interpretation are shown as black lines, full details can be found in *Smith and Murray* [2009]. Array 1 (west) lies above a more solid "sliding" bed and Array 2 (east) is over a 'deforming' bed. A kinematic GPS station is colocated with the center of Array 1 (blue triangle). Inset: Location of Rutford Ice Stream indicated by red box.

how investigating multiple aspects of basal microseismic data in ice can provide new spatial and temporal constraints on the variable conditions at the base of the ice stream. These results are compared to bed properties determined from independent seismic reflection and radar studies [*King et al.*, 2009; *Smith and Murray*, 2009] collected in the area, demonstrating the strength in combining multiple geophysical techniques for a robust interpretation.

2. Survey Location and Data Collection

Rutford Ice Stream is a fast-flowing ice stream located in West Antarctica (Figure 1). The average ice-flow speed is 377.3 m a^{-1} [*Murray et al.*, 2007], and the ice stream drains ~49,000 km^2 of WAIS into the Ronne Ice Shelf [*Doake et al.*, 2001]. The area covered by this survey is approximately 40 km upstream from the grounding line, the location where the ice stream becomes a floating ice shelf. In the survey region the ice is ~2.2 km thick with around 1.9 km of this lying below sea level. The ice stream is bounded by the Ellsworth Mountains to the west and the Fletcher Promontory to the east.

Ten three-component 4.5 Hz GS-11D geophones were deployed over a 34 day period during the austral summer of 2008/2009. Each geophone was connected to a data logger (3 × REFTEK RT-130 and 7 × ISSI SAQS) sampling at 1000 samples per second, a battery, solar panel, and GPS for timing (ensuring the relative timing on each station is synchronized). Geophones were orientated with the horizontal components pointing in the direction of flow and across the flow, toward the Ellsworth Mountains (Figure 1). They were buried around 1 m below the surface to ensure good coupling and to reduce environmental noise.

The recording stations were configured into two adjacent cross arrays (Figure 1) over areas of the bed that have been previously interpreted as having contrasting bed types from independent studies [*Smith*, 1997b; *Smith and Murray*, 2009] using active source seismic methods. In those studies a number of seismic reflection lines (Figure 1) in the same area as our passive seismic arrays have been used to derive the reflection coefficient of the ice-bed interface, allowing the acoustic impedance (the product of seismic velocity and density) of the bed to be determined. This indicated that over the whole region, the bed material is soft, water-saturated sediments. In some places these sediments are interpreted as high porosity (e.g., >0.4) and deforming pervasively with the movement of the overriding ice; elsewhere, porosity is lower, and sliding of the ice over the bed is more significant than sediment deformation. The boundary between these two bed types was mapped from the seismic data [*Smith and Murray*, 2009] and extended further on the basis of more detailed bed topography and reflectivity from radar surveys [*King et al.*, 2009]. Full details of the seismic and radar methods are given in *Smith* [2007], *Smith and Murray* [2009] and *King et al.* [2009].

Array 1 (west) was located over an area with an inferred low-porosity ($\leq$ 0.3), consolidated basal till, where motion is primarily by basal sliding. Array 2 (east) was over an area with an inferred high-porosity (> 0.4) dilatant till which deforms pervasively. The two array centers were 4.5 km apart, and the interstation spacing was 1 km. A dual-frequency GPS receiver was colocated with the central station in Array 1 to record surface motion of the ice stream (Figure 1). The area is covered by a dense basal topography grid (node spacing 50 m × 50 m) determined by RES with a vertical resolution of ±3 m [*King et al.*, 2009].

3. Event Detection and Location

3.1. Automated Location Process

During the 34 day recording period tens of thousands of basal seismic events were observed, with overlapping events occurring every few seconds. Many of these events produced very low amplitude seismic waves, close to background noise levels that were only visible on a single station. In order to accurately locate an event, the arrival waveform must be identifiable across several stations. To achieve this, only events that produced arrivals that could be detected on at least four stations with signal-to-noise ratios (SNR) of greater than nine (determined by testing on several sections of the data) were used in this study: 2967 good quality basal microseismic events meeting these criteria were detected over the recording period. Automated detection and location of such events was achieved using the coalescence microseismic mapping (CMM) technique [*Drew et al.*, 2013]. The CMM technique allows the detection and location of events without reducing data to discrete arrival time picks. Given the nature of this data set, with overlapping events, this method allows coherent arrivals across the 10 stations to be identified, reducing "false triggers" from seismic energy unrelated to a given event.

The CMM technique works by continuously migrating an envelope of seismic energy from each recording station back to each node in a three-dimensional subsurface grid (node spacing 150 m × 150 m × 50 m). A coalescence function is calculated at each grid node over time, and a peak in this function indicates a location and origin time that best fits the observed seismic data, indicating a likely time and location of a microseismic event. This process is performed for both *P* wave and *S* wave arrivals, with *P* wave energy being detected on the vertical component and *S* wave energy on the combined horizontal components. The migration is performed by using a 1-D seismic velocity model to forward model *P* wave and *S* wave travel times from each node in the 3-D subsurface grid to each recording station.

The 1-D *P* wave velocity model contains a firn layer in the top 100 m, with a mean velocity of 2839 ± 15 m s^{-1} derived from *P* wave velocities determined by shallow refraction surveys, detailed in *Smith* [1997a]. Below this a mean ice column velocity of 3841 m s^{-1} [*Smith*, 1997a] was determined using the relationship between ice temperature and seismic velocity [*Kohnen*, 1974]. We did not insert a velocity step at the ice-bed interface as the velocity and depth of that region is not well constrained, and a sharp step in the model can cause
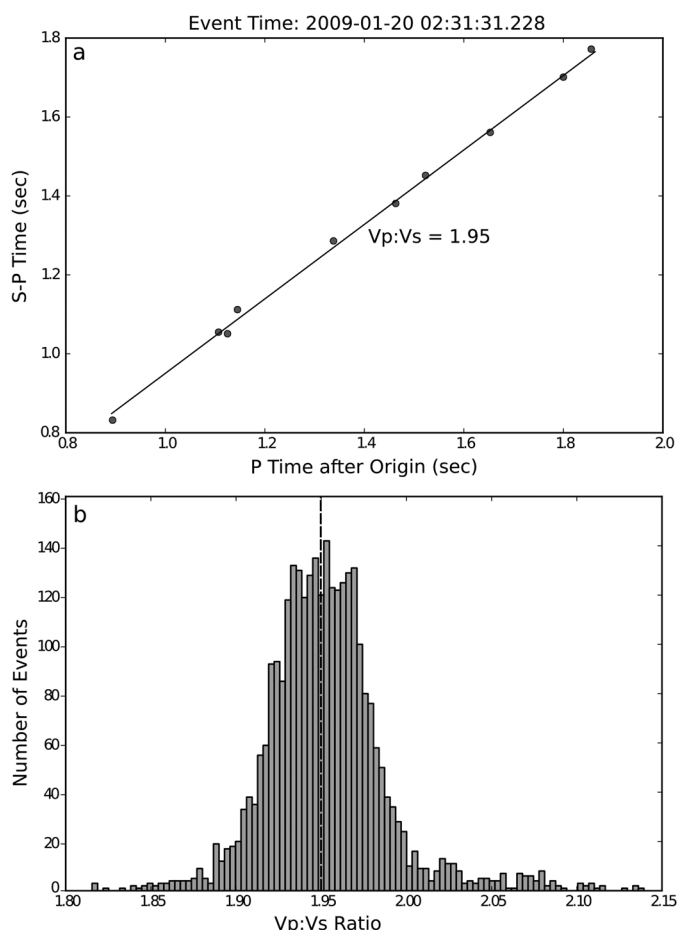
Figure 2. V_p:V_s ratio of seismic velocities. (a) Typical Wadati plot for a single event, showing P wave arrival time verses S-P time difference for each station. The gradient of the line fitting these points is used to calculate the V_p:V_s ratio. (b) Histogram of V_p:V_s measurements for 2967 events, measurements have a mean of 1.95 ± 0.04.

artificial clustering of hypocenters at the depth of the step. A constant V_p:V_s ratio of 1.95 was calculated using Wadati plots [*Wadati*, 1933] of P wave and S wave arrival times (Figure 2) and agrees well with values of *Roethlisberger* [1972].

A typical event of the quality described above is shown in Figure 3. The P wave arrival is impulsive with a dominant frequency of around 130 Hz, typical of basal seismicity [*Anandakrishnan and Bentley*, 1993]. The S wave arrival is often "split," appearing at slightly different times on the two horizontal components, due to the presence of anisotropy in the seismic velocity structure of ice. The fastest S wave arrival (S1) was always used in this study.

The CMM technique was an efficient means of quickly processing a large data set, to identify and approximately locate good quality microseismic events. These locations were then refined by the following automated process (Figure 4). First, P wave and S wave arrival time picks for each station were tuned (i.e., adjusted to more consistently identify the onset of the seismic arrival) by calculating the SNR in a limited window, 50 ms either side of the CMM arrival times. This produced a more precise and consistent onset pick (the time at which the wavelet arrival begins) for each event at each station. Using these tuned arrival times, the location of each event was recalculated using a probabilistic, nonlinear earthquake location technique (NonLinLoc) [*Lomax et al.*, 2000]. This technique works by calculating a probability misfit between theoretical modeled arrival times and observed arrival times at each station from each node within a 3-D subsurface grid; a minimum in this function (i.e., the highest similarity between modeled and observed arrival times) indicates a maximum likelihood origin time and location. Independently, travel time picks were further improved by cross-correlating P wave arrivals to identify similarities between the waveforms at each station. Finally, the refined locations
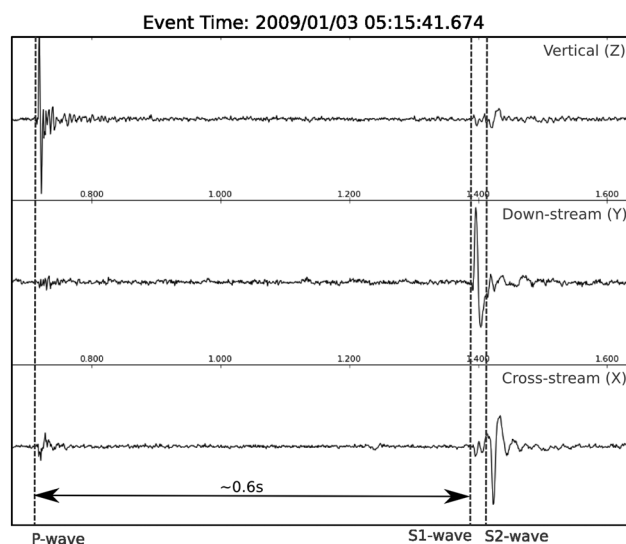
Figure 3. Typical basal seismic event recorded on all three components of a single station. Dashed lines indicate *P* wave and *S* wave arrivals. Events are characterized by a high-frequency impulsive *P* wave (130 Hz) on the vertical component (*Z*) and strong shear waves which exhibit shear wave splitting (S1 and S2) on the horizontal components (*Y* and *X*). The vertical axis for each trace is the same and is in instrument counts; the horizontal axis is time.

(from NonLinLoc) and *P* wave cross correlations were input to a double-difference, relative location technique (HypoDD) [*Waldhauser and Ellsworth*, 2000]. This technique exploits the fact that events that are spatially close will have very similar travel paths; thus, differences in their travel times to a given station can be attributed to the spatial offset between events independent of velocity model errors. This process serves to improve relative locations within clusters of events that are spatially close and have similar waveforms.

3.2. Event Locations

Figure 5 gives an overview of the locations of the 2967 good quality events observed over the 34 day recording period. The topography of the ice-bed interface is shown for reference [*King et al.*, 2009]. A plan view of the seismicity (Figure 5a) reveals that events are concentrated in spatial clusters. An individual cluster consists of many events occurring

in close proximity to each other, with a near identical waveform at a given receiver throughout the 34 day recording period (Figure 5c gives an example of three such events from one cluster). This indicates that events within a cluster are highly likely to come from a single failure point or "sticky spot." Seismicity at a cluster location turns on and off over time suggesting that a sticky spot activates repeatedly. The range of time for which a cluster is active, and the total number of events within a cluster varies across the survey area. Some clusters are active in bursts of several hours over the full 34 day recording period, for example, the cluster in

Figure 5c, which compromises of 101 events. At the other end of the scale we see clusters that are active just once, with ~10 events in total.

Vertical profiles (Figure 5b) confirm that the seismicity is close to the ice-bed interface. Figure 5b gives the appearance that events seem to originate from both above and below this boundary in vertical "pipe-like" features. Clusters on the right hand side (downstream) of profile Y-Y' appear to be located within the ice, whereas events in the center and to the left-hand side (upstream) of the profile appear to occur around the interface. Given the previous observation that events within a cluster have a consistent waveform at a given receiver, suggesting a consistent source mechanism, it is unlikely that the events in a single cluster lie both above and below the ice-bed interface. It is therefore important to determine the origin of these observed pipe-like features. Waveforms between
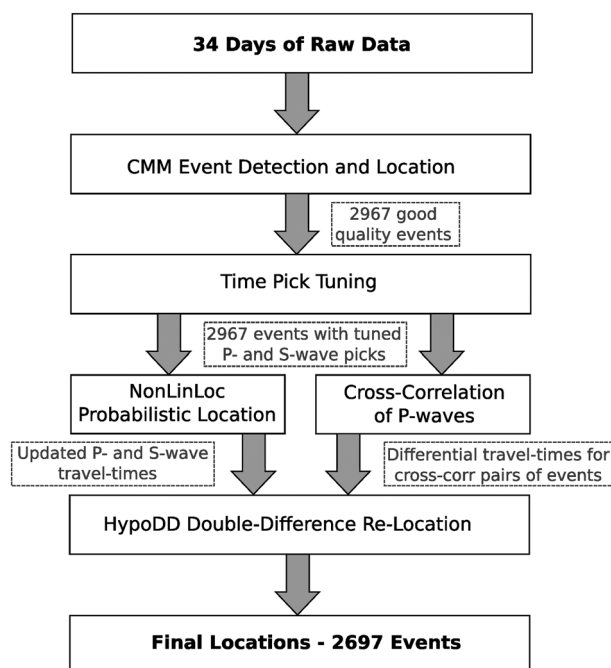

Figure 4. Automated location process flow chart from raw microseismic data to final event locations (Figure 5).
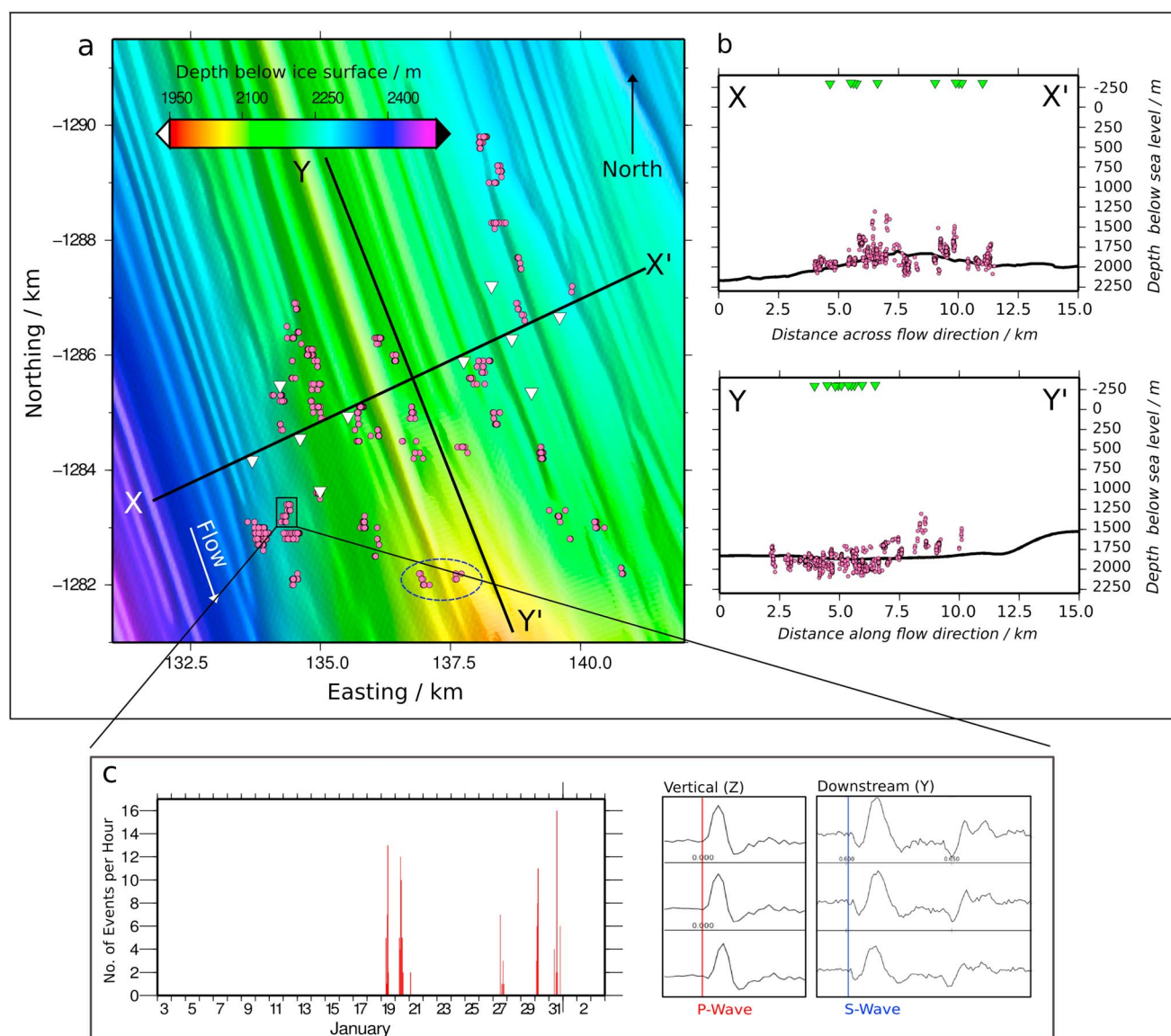
Figure 5. Location of 2967 basal seismic events. (a) Plan view of event locations (pink) showing spatial clustering, many events are overlayed on top of each other. Seismic stations are shown in white, and the colored underlay is the depth of the ice-bed interface below the ice surface determined from RES. (b) Vertical profile (top) across flow direction and (bottom) along flow direction showing events in vertical pipe-like features. The black line marks the ice-bed interface from RES data. All events are projected onto a profile through the ice-bed interface. The blue boxes indicate the cluster in Figure 5c that is further analyzed. (c) Cluster characteristics: a single cluster turns on and off over the recording period (left); the waveforms for three events within one cluster the vertical scale on each event is the same, so amplitudes can be compared between events. Waveforms show a high degree of similarity; this is true for all 101 events in this cluster and for all other clusters, suggesting that the source of seismicity is the same for all events within one cluster.

clusters also show a high degree of similarity (Figure 5c) suggesting that each cluster is generated within the same source material, although we cannot determine from depth distribution alone whether this is the ice, the interface, or the bed material.

Due to the presence of strong shear wave arrivals, events cannot have originated from beneath a significant basal water layer; they are also unlikely to have come from a significant distance (e.g., more than 50 m) above the interface as we would expect to see reflected or converted arrivals after the primary *P* wave and *S* wave arrivals. The average duration of a *P* wave arrival is 0.01 s. The travel time difference for a *P* wave that originates 50 m above the interface, at 4.5 km offset, is 0.01 s, so we cannot distinguish a reflected arrival from this depth, or below, from the primary arrival.
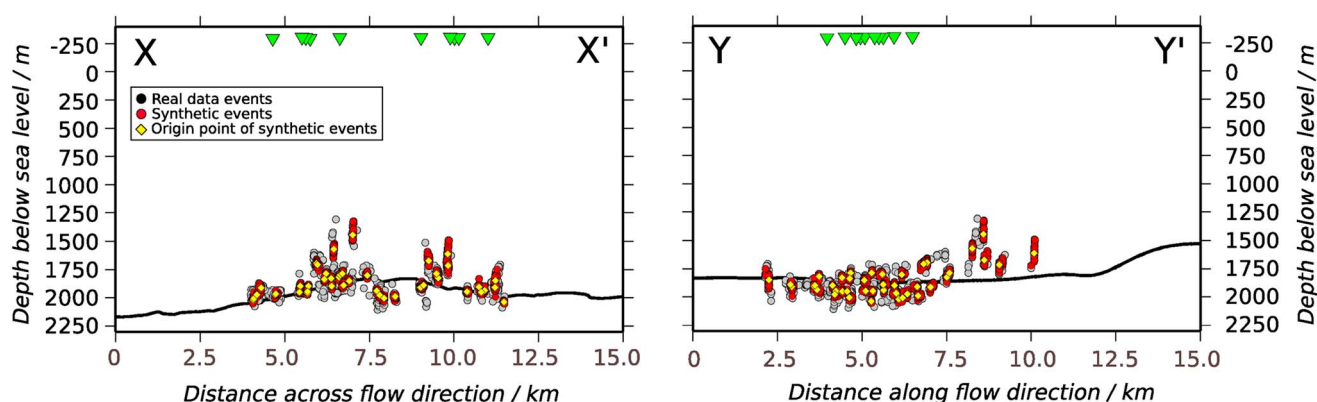
Figure 6. Testing the effect of survey geometry on depth location. Real data events are shown in grey and are the same as those in Figure 5b, synthetic event locations are shown in red. Synthetic events originated from a single point at the center of each cluster (yellow). When located with a small amount of random noise added to the time picks at each station they exhibit the same pattern as the real data, with an apparent origin in vertical pipe-like features that straddle the ice-bed interface. These pipe-like feature become increasingly elongated outside the seismic array (seismic stations shown in green). This suggests that the same is true for the recorded data and that events within a single cluster originate from a single failure point.

3.3. Location Uncertainty

In order to determine the resolution of the location method used, we have performed a number of tests using synthetic seismic events with a known origin time and location and located them using the same method as the field data, described in section 3.1. Two tests were designed to investigate the effects of survey geometry and velocity model errors on event location. In particular, we want to constrain the depth resolution of our data; thus, our constraint on the hypocentral depths in order to determine whether the events originate from within the ice, at the interface or within bed material.

Using NonLinLoc, synthetic tests can be performed by generating multiple events at a given location using the velocity model described in section 3.1. Arrival times for each synthetic event then have a random Gaussian timing error added, to mimic a realistic mispick of up to three samples (i.e., 0.003 s) for *P* wave picks and five samples (i.e., 0.005 s) for *S* wave picks. These arrival times are then used to locate the synthetic events and derive output locations, following the same steps as used for the recorded data.

The first test was designed to investigate the effect of survey geometry on event locations, specifically whether this could be the cause of observed pipe-like features. Fifty synthetic events were generated at the center of each of the location clusters observed in the recorded data, giving 2200 synthetic events in total. The yellow diamonds (Figure 6) show the true origin of the synthetic events. When located using the same velocity model with which they were created the resulting distribution of synthetic arrivals exhibit a similar pattern to the recorded data, appearing to originate from vertical pipe-like features crossing the ice-bed interface. These features become increasingly elongated toward the edges and outside the geophone arrays. For a single cluster, synthetic events all originated from a single point and were created and located with an identical velocity model. Therefore, the vertical spread in their apparent locations is probably a result of the survey geometry interacting with the arrival time errors. When combined with the observation from the field data of nearly identical waveforms within a cluster, this is compelling evidence that the real events originate from discrete failure points associated with each individual cluster rather than from across a significant vertical range.

The second suite of tests was designed to determine whether velocity model errors could account for the distribution of clusters of events both in the ice and at the interface and whether this spatial distribution is likely to be a real feature. As with the previous test, clusters of 50 synthetic events were created but this time at the ice-bed interface underneath each of the recorded data clusters. These synthetic events were then located with velocity models that varied from +5% to −5% of the velocity model they were created with and also located with velocity models that had a $V_p:V_s$ ratio of 1.9 and 2.0 (0.05 lower and higher, respectively, than the velocity model with which they were created). Figure 7 shows the result of locating these clusters with a velocity model 3% higher than that with which the synthetics were created, illustrating the situation where the chosen velocity model for Rutford Ice Stream is higher than that preferred. The majority of synthetic events exhibit a similar pattern to the recorded data with event clusters outside the geophone arrays being located upward and outward from their true position. The effect is increased with increasing distance and
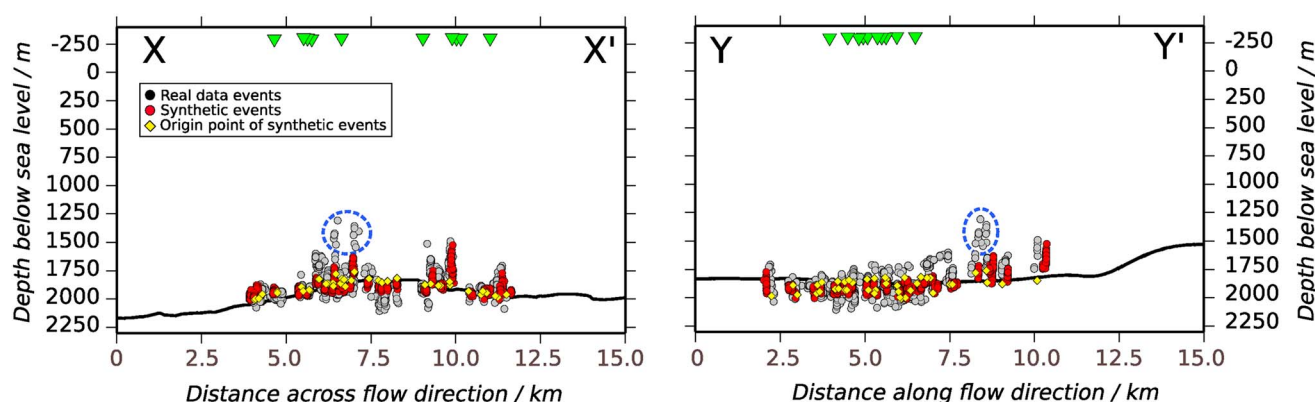
Figure 7. Testing the effect of survey geometry and velocity error on depth location if events are assumed to originate at the ice/bed interface. Real data events are shown in grey and are the same as those in Figure 5b, synthetic event locations are shown in red. Synthetic events originated from the ice-bed interface directly underneath each cluster; origin points are shown in yellow. The ice-bed interface (black line) is a 2-D profile taken through the 3-D interface shown in Figure 5a; therefore, some of the yellow diamonds do not appear to plot at this interface because they are off this profile. When synthetic events are relocated with a small amount of random noise and a velocity 3% higher than that with which they were created, the majority of them exhibit the same pattern as the real data. This suggests that events that appear in the ice could have originated from the ice-bed interface, with the exception of the events circled in blue, which are also circled in Figure 5a.

hence angle of arrival at the geophones. This suggests that a small velocity model error combined with a small arrival time error is a likely explanation for this vertical pattern of event clusters. In most cases events are likely to be from the ice-bed interface, despite appearing to be located within the ice toward the edges and outside of the geophone array.

A small number of event locations that appear to be within the ice, around 300 m above the bed, cannot be explained by these tests (events inside the blue circle in Figures 7 and 5a). Closer inspection of these events shows that the time picks are good and that the waveforms, source mechanisms, and V_p:V_s ratios are similar to the other events within the survey. The waveforms show no evidence of reflections or converted arrivals from the ice-bed interface, which would be expected ∼0.07 s after the primary P wave arrival for events 300 m above the bed. There is no simple conclusion as to whether these events truly originate from within the ice; they are in an area where the ice stream bed topography rises sharply, and it remains possible that we are seeing englacial seismicity associated with this.

We find that the best resolution of the location method with the given array configuration is ±20 m in the horizontal direction and ±32 m in the vertical. This was determined by looking at the location spread of a cluster of 50 synthetic events in the center of the survey area from the first test. All events in a cluster originate from the same point, so the distance of their apparent location from this origin point indicates the magnitude of errors expected from the location method. In some cases the error may be larger than this, particularly for events outside of the geophone arrays. This number does not account for potential errors in the velocity model. The horizontal error in event locations is of a similar order to the total movement of the sensors on the surface of the ice stream during the 34 day recording period (∼35 m); we have not corrected for the daily motion of recording stations, so this effect is incorporated within the errors.

This analysis highlights the poor resolution of the depth location of events from this array configuration, and the sensitivity of location to the velocity model. It should also be noted that the seismic velocity of ice is known to be highly anisotropic. A study using a section of the data set referred to in this paper determined S wave anisotropy to be as high as 6% in this area of Rutford Ice Stream [*Harland et al.*, 2013]. Therefore, the use of an isotropic velocity model in this study will introduce some location error. Caution must therefore be exercised when using event depth to inform the exact source of seismicity with respect to the ice-bed interface.

3.4. Event Timing

In this area the surface velocity of Rutford Ice Stream varies due to stress transmission of tidal forcing upstream of the grounding line (Figure 1). This variation is dominated by a periodic cycle of 14.77 days, causing a velocity variation along flow of around ±10% [*Murray et al.*, 2007; *Gudmundsson*, 2006]. It would follow that the changing basal stress causing this velocity variation might be visible in the levels of basal seismicity. *Adalgeirsdóttir et al.* [2008] observed that in this area of Rutford Ice Stream, the highest levels of basal
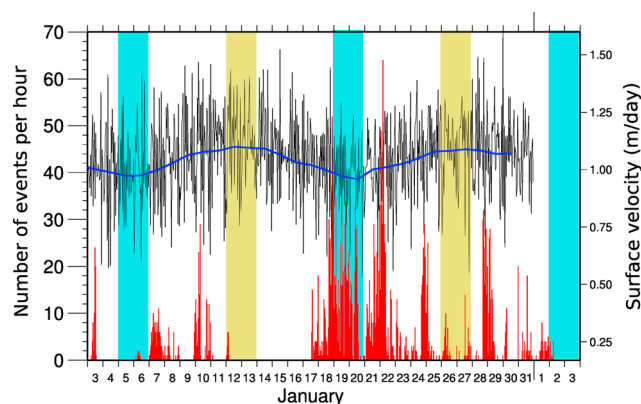
Figure 8. Histogram of the 2967 good quality events observed over the 34 day recording period, events are binned in number of events per hour (left axis) and the surface velocity of the ice stream (right axis) determined from surface GPS data. The surface velocity is sampled once per hour (black). The blue line highlights the long wavelength cyclicity of 14.77 days; spring tides at the grounding line are highlighted in yellow and neap tides in blue. The level of seismicity through time shows no clear pattern relating to the changing surface velocity.

seismicity correlated with spring tides, when the velocity is highest, and that there are often two peaks in both seismicity and velocity during a diurnal tidal cycle.

A temporal view of the 2967 good quality events observed over the 34 day recording period (Figure 8) does not show a clear pattern. Seismicity occurs in bursts, but there is no regular periodicity or event rate cyclicity. In particular, there is no correlation with the dominant fortnightly spring/neap variation in surface velocity of the ice stream (Figure 8), determined from the surface GPS station. In fact, the highest levels of seismicity occur between 18 and 22 January, during a neap tide. When the levels of seismicity were inspected for peaks during each diurnal period, there was again no obvious sign of a regular number of peaks per cycle.

It is not clear why our observations of event timing differ from the findings of *Adalgeirsdóttir et al.* [2008]. It may be related to the fact that the event detection and location methods differed considerably between the two studies, although it is clear in both cases that events are from the ice-bed interface region. The microseismic data presented by *Adalgeirsdóttir et al.* [2008], from a study by *Smith* [2006], were acquired using different recording equipment and acquisition parameters than our data, particularly in station spacing, geophone response, and logger sampling rate (see *Smith*, 2006, for details). They also used a simpler and very different event detection method. The field data recorded by *Smith* [2006] was triggered by high-amplitude *P* wave arrivals only; event identification in post-processing was based only on a count of the number of events detected at each individual station within an array rather than the detection of coherent energy across a number of stations as used in this study. It is therefore possible that the different methods used resulted in different subsets of the total microseismic activity being selected in the two different studies. It also remains possible that the dynamics of this area have changed over the time between these two studies.

4. Fault Plane Solutions and Source Parameters

In order to investigate the seismic source mechanism that is responsible for generating basal microseismic events, fault plane solutions (FPS) were constructed for a representative event in each cluster using the first motion of *P* wave arrivals at each station. The polarities at each station (compressional or dilatational) were plotted on a lower hemisphere stereographic projection. A double-couple model was assumed in order to separate the focal sphere into compressional and dilatational quadrants using two orthogonal nodal planes, the fault plane and the auxiliary plane, using the program FPFIT [*Reasenburg and Oppenheimer*, 1985]. It is not possible from the FPS alone to determine which of these nodal planes is the fault plane. Figure 9b shows a typical lower hemisphere FPS; the *P* wave first motion polarity picks are of excellent quality and unambiguous. The most likely fault plane and auxiliary plane are marked, indicating a low-angled thrust fault slipping in the ice flow direction. The alternative would be a near-vertical fault slipping across the flow direction, which is physically unlikely. The dip and strike of the fault plane are not tightly constrained. However, the slip vector to this plane is tightly constrained by the auxiliary plane, giving a consistent indication of low-angled slip in the ice flow direction. Across the survey area we see a consistent source mechanism of low-angled (likely subhorizontal) faulting, slipping within $\pm 10°$ of the ice flow direction (Figure 9). The polarity of the FPS is consistent with the upper block (glacial ice) moving southward with respect to the lower block (basal till). This further supports the conclusions that the mechanism of failure for each location cluster is the same and also implies that events identified as originating from above the ice-bed interface in section 3.3 could be at the interface, rather than within the ice. The pattern of low-angled faulting in the ice-flow direction is consistent with the findings of *Anandakrishnan and Bentley* [1993] on Ice Stream C, Antarctica.
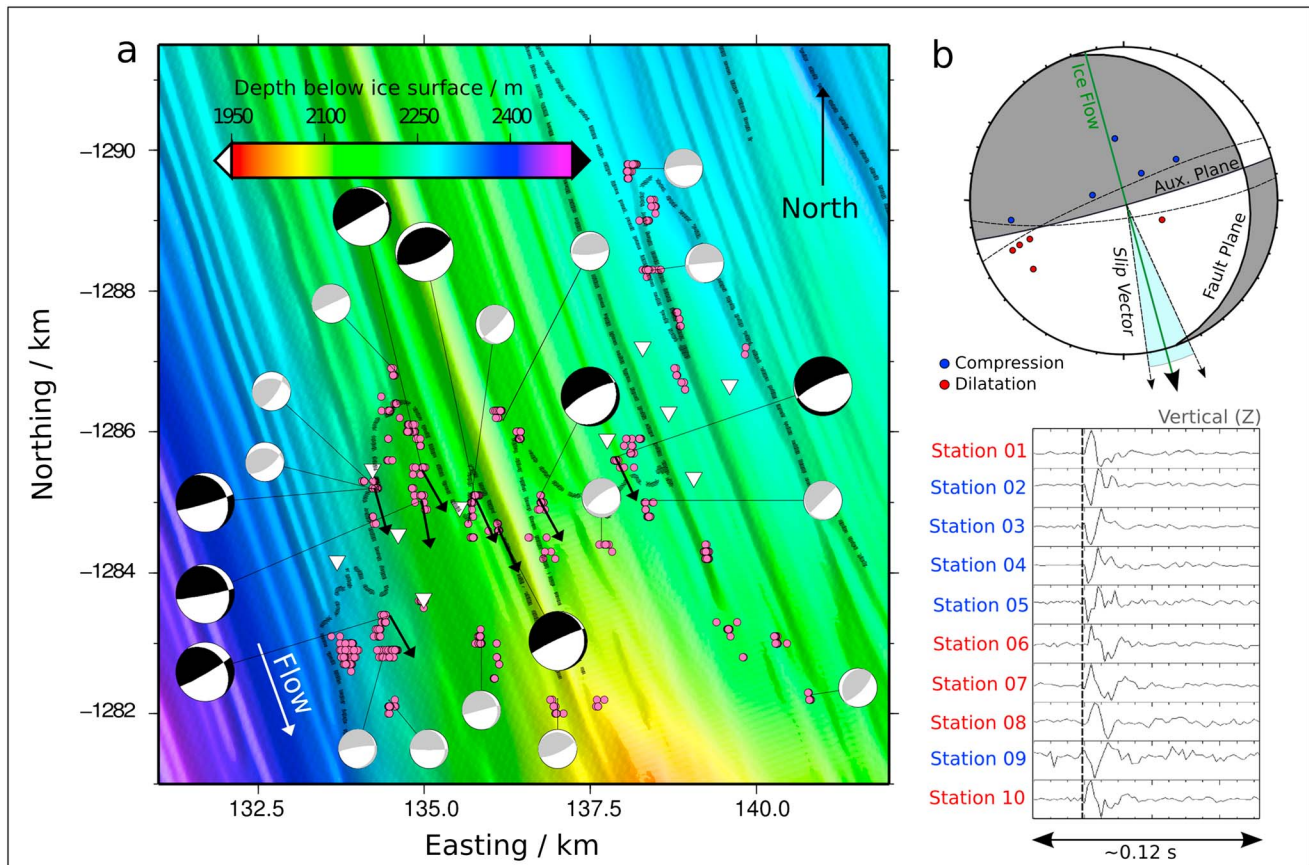
Figure 9. Fault plane solutions. (a) Fault plane solutions for a representative event in each cluster, constructed by picking first motion *P* wave polarities. Large black solutions are those that are well constrained, and the corresponding slip vectors are shown. Small grey solutions are less well constrained but are shown for completeness. The pattern of low-angled faulting in the ice flow direction is consistent across the survey area. The dashed line indicates the interpreted boundary between stiff basal till and dilatant basal till (G. Boulton, personal communication, 2015), determined from independent studies of seismic reflection and radar data [*Smith and Murray*, 2009; *King et al.*, 2009]. Areas of seismicity largely coincide with the stiff basal till areas (south of the boundary). (b) A typical (top) lower hemisphere fault plane solution; compressional quadrants (downward first motion) are shaded. The dashed lines show the limits of the auxiliary plane, and the corresponding region of possible slip vectors is shaded in blue. The fault plane is low angled, and its strike is not well constrained. The slip vector constrained by the auxiliary plane is well constrained and is in the ice flow direction. (bottom) *P* wave polarities are clear and unambiguous.

An estimate of the seismic scalar moment of a typical event was obtained using an implementation by *Walter et al.* [2009] of the linear time domain moment tensor inversion scheme used by *Dreger et al.* [2000] and *Dreger and Woods* [2002]. The event chosen was located in the center of the survey area to optimize focal sphere coverage. Green functions were computed using the F-K software developed by *Zhu and Rivera* [2002]. The 1-D velocity model used in the event location was employed with seismic quality factor $Q_p = 350$ [*Peters et al.*, 2012]. Although fault plane orientations are not well constrained by the inversion, due to poor focal sphere coverage, the scalar moment is robust and varies little when different numbers of stations are included. The seismic moment (M_0) for this single microseismic event is 6×10^6 Nm giving a moment magnitude of $M_w = -1.48$ (using equation (1)) [*Hanks and Kanamori*, 1979].

$$M_w = \frac{2}{3} \log_{10}(M_0) - 6 \qquad (1)$$

The magnitude of all 2967 events can be determined on a local scale (M_R) for this area and tied to the moment magnitude (M_w), using equation (2) which follows the general form of magnitude scales [*Lay and Wallace*, 1995].

$$M_R = \log_{10}(Amp) + 0.21x - 4.69 \qquad (2)$$

For each event the maximum amplitude (in instrument counts) of the *P* wave arrival at each station was measured (Amp) and a distance correction (in km) to account for the hypocentral source to receiver distance (*x*)
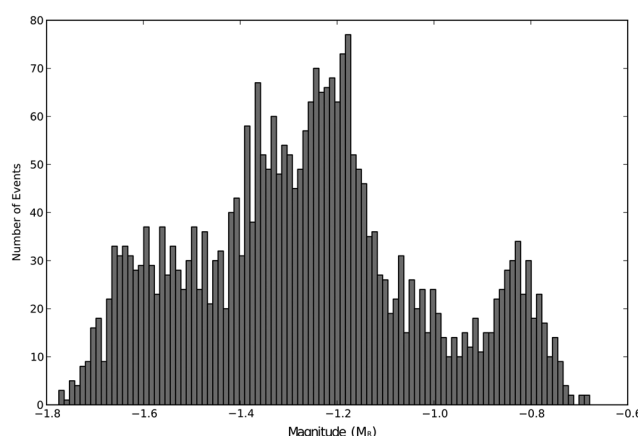
Figure 10. Histogram of the magnitudes (M_R) of the 2967 good quality events observed over the 34 day recording period, events are binned at intervals of 0.01. The tail off of events with $M_R < -1.48$ is typical and due to the limitation on detecting smaller magnitude events. The upper limit of magnitude $M_R = -0.67$ suggests a maximum seismic moment of $M_0 = 9.6 \times 10^7$ Nm.

was added. The distance correction term $0.21x$ was derived by linear regression of the relationship between x and $\log_{10}(\text{Amp})$. The mean of the M_R measurement at each station was taken to calculate the final M_R for an event. A scaling factor of -4.69 was determined by comparing the value of M_R to the value of M_w determined for the event above and serves to tie the two scales at this point. An estimate of the seismic scalar moment for a second event was determined using the method of *Walter et al.* [2009] described above, to provide a validation of the M_R magnitude scale. A value of $M_W = -0.69$ was determined, compared to a value of $M_R = -0.89$ for the same event.

A histogram of the magnitudes for all events (Figure 10) displays a range of $-1.77 < M_R < -0.68$. The drop off in number of events with $M_R < -1.48$ is typical and due to event detection limits of smaller magnitude events. The upper magnitude limit, $M_R = -0.67$, equates to a maximum seismic moment of $M_0 = 9.6 \times 10^7$ Nm. This is significant as it suggests this is the maximum amount of energy that can be released by seismic failure on a sticky spot. We can calculate the amount of displacement for an event of this magnitude using equation (3) [*Aki and Richards*, 2002].

$$M_o = \mu A D \qquad (3)$$

If we take a value of rigidity between that of ice and till, $\mu = 2.73 \times 10^9$ Nm^{-2} [*Anandakrishnan and Bentley*, 1993] and assume a fault area (A) of 1 m^2, we get a fault displacement (D) of 35.15 mm. The choice of a fault area of 1 m^2 is consistent with the expected fault displacement-length scale relationship proposed by *Cowie and Scholz* [1992].

Calculating the displacement for all 2967 events, gives a range of 0.80 mm $< D <$ 35.15 mm displacement for an individual event. Hence, the amount of motion taken up by seismic deformation is small and suggests that the ice stream motion over a sticky spot happens by both seismic and aseismic deformation.

5. Discussion

The spatial pattern of seismicity from the base of Rutford Ice Stream shows that events are confined to discrete areas near the ice-bed interface, where the motion of the overlying ice stream is accompanied by seismic failure. In addition, these discrete sticky spots fail repeatedly over time in the same manner, with fault plane solutions consistent with low-angled faulting, slipping in the ice-flow direction. The ice-bed interface of Rutford Ice Stream has not been directly observed, but it is likely to be a complex zone rather than a discrete discontinuity, where basal ice and till interact and to some extent could be mixed. It is not possible to tell from the depth resolution of these data exactly where the seismicity originates, although they do locate it within the vicinity of the ice-bed interface. The presence of strong shear wave arrivals means events cannot have traveled through a significant amount of water beneath the ice, and the absence of reflected or converted arrivals indicates that they did not originate above the ice-bed interface. As our synthetic testing shows that events within a cluster are likely to come from a discrete failure point, we therefore conclude that this is most likely to be at the ice-bed interface rather than in the ice or the bed. One possible exception to this is the small number of events that appear to originate within the ice (Figures 7 and 5a), although the fact that the waveforms, source mechanisms and $V_p : V_s$ ratios are similar to the other events within the survey suggests that even these events may actually still come from the ice-bed interface.

A mechanism that fits these observations is that these are areas where Rutford Ice Stream is moving by basal sliding of ice over a stiff consolidated till. It therefore follows that areas outside these sticky spots are

accommodating ice stream motion aseismically, probably by pervasive deformation of dilatant tills underlying Rutford Ice Stream or by sliding over a well-lubricated stiff bed. Furthermore, when the location of sticky spots are compared with a boundary between stiff and dilatant basal till areas (G. Boulton personal communication, 2015), mapped from independent studies using seismic reflection and radar data [*Smith and Murray*, 2009; *King et al.*, 2009], it can be seen that the microseismic sticky spots coincide with areas identified as stiff till (Figure 9). The dashed line in Figure 9 indicates the boundary between stiff and dilatant till, with the stiff till areas lying to the south of this boundary. The majority of sticky spots fall inside the stiff till areas and many are located at, or close to, the boundary between the contrasting till types. This pattern suggests the change in basal conditions, and sliding characteristics at this boundary may play a role in initiating the seismicity.

From a preliminary passive seismic survey in this area, *Smith* [2006] concluded that parts of the ice stream likely to be moving by basal sliding showed levels of seismicity 6 times greater than those moving over a deforming bed. This conclusion was drawn from a simple count of the number of events detected at stations situated over the two different bed types and provided only weakly constrained locations of seismic events. Our present study shows that the basal dynamics of this area are much more complex. By determining event locations and source mechanisms we can see a distributed pattern of basal sliding and bed deformation. Cross referencing this with seismic reflection data also confirms this interpretation and highlights the use of passive seismics as a technique to map and investigate basal dynamics.

It has been shown that a strong ($\pm10\%$) periodic variation in ice surface velocity in this area is caused by tidal forcing [*Murray et al.*, 2007; *Gudmundsson*, 2006]. This indicates that a strong periodic variation in basal stresses, resisting ice flow, exists. Therefore, a reflection of this in the levels of basal seismicity would also be expected, as has been demonstrated on other Antarctic ice streams [*Anandakrishnan and Alley*, 1997]. The lack of this correlation between surface velocity and basal seismicity levels in Rutford Ice Stream indicates that the sticky spots in this area are unaffected by changes in basal stress. The displacement due to seismic failure on a sticky spot at the base of Rutford Ice Stream is small. Analysis suggests that a slip of 35.15 mm is the upper limit of the amount of surface motion that can be accommodated by individual slip events on a sticky spot. This implies that much of the motion of Rutford Ice Stream is taken up aseismically, unlike other ice streams where stick slip on large-scale sticky spots is the dominant motion [*Wiens et al.*, 2008; *Winberry et al.*, 2013]. It could also suggest that it is this material, deforming aseismically, that is subject to alterations in stress due to tidal forcing. *Thompson et al.* [2014] suggest a mechanism for the transmission of stresses upstream of the grounding line by tidally modulated changes in till pore pressure, causing a slow down or speed up of the ice stream. This model is consistent with our suggestion that changes in the aseismic dilatant till are responsible for surface velocity changes and that the sticky spots' formed of stiffer till, are not affected by these changes.

6. Conclusion

We have used passive microseismic monitoring on Rutford Ice Stream to locate ~3000 good quality basal seismic events over a 34 day period using an optimized automated detection and location process. Events are concentrated in spatial clusters that turn on and off over the recording period with source mechanisms consistent with low-angled faulting in the ice flow direction. The clusters are interpreted to occur at sticky spots of stiff basal till at the ice-bed interface, where ice movement is accommodated by stick slip basal sliding. The sticky spots coincide with areas identified as stiff basal till from an independent study using seismic reflection surveying and many of them occur close to the interpreted boundary between stiff and dilatant till. The displacement on the fault planes is taking up only a small amount of the overall motion of the ice stream, suggesting that the majority of movement in this area is accommodated by pervasive aseismic deformation. The seismicity shows no correlation with tidally modulated surface velocity variations, suggesting a possible mechanism for transmitting tidal stresses upstream of the grounding line is through changes in the pore pressure of the dilatant till.

These results highlight the value of passive seismic techniques, especially if combined with more traditional active seismic and radar methods, to provide an interpretation of the material characteristics of an ice stream bed. Microseismic monitoring proves to be an effective tool for investigating both the spatial and temporal basal dynamics that accommodate ice stream motion; using this technique, we have added new and complementary information to a well-studied area of Rutford Ice Stream. Passive microseismic monitoring of signals generated at the base of fast-flowing ice streams can greatly increase our understanding of the ice-bed interface characteristics in these regions.

References

Adalgeirsdóttir, G., A. M. Smith, T. Murray, M. A. King, K. Makinson, K. W. Nicholls, and A. E. Behar (2008), Tidal influence on Rutford Ice Stream, West Antarctica: Observations of surface flow and basal processes from closely spaced GPS and passive seismic stations, *J. Glaciol.*, *54*, 715–724, doi:10.3189/002214308786570872.

Aki, K., and P. G. Richards (2002), *Quantitative Seismology*, Univ. Sci. Books, Sausalito, Calif.

Alley, R. B. (1993), In search of ice-stream sticky spots, *J. Glaciol.*, *39*, 447–454.

Anandakrishnan, S., and R. B. Alley (1997), Tidal forcing of basal seismicity of ice stream C, West Antarctica, observed far inland, *J. Geophys. Res.*, *102*, 15,183–15,196, doi:10.1029/97JB01073.

Anandakrishnan, S., and C. R. Bentley (1993), Micro-earthquakes beneath ice streams B and C, West Antarctica: Observations and implications, *J. Glaciol.*, *39*, 455–462.

Bamber, J. L., D. G. Vaughan, and I. Joughin (2000), Widespread complex flow in the interior of the Antarctic Ice Sheet, *Science*, *287*, 1248–1250, doi:10.1126/science.287.5456.1248.

Blankenship, D. D., C. R. Bentley, S. T. Rooney, and R. B. Alley (1986), Seismic measurements reveal a saturated porous layer beneath an active Antarctic ice stream, *Nature*, *322*, 54–57, doi:10.1038/322054a0.

Blankenship, D. D., S. Anandakrishnan, J. Kempf, and C. R. Bentley (1987), Microearthquakes under and alongside ice stream B, Antarctica, detected by a new passive seismic array, *Ann. Glaciol.*, *9*, 30–34.

Cowie, P. A., and C. H. Scholz (1992), Displacement-length scaling relationship for faults: Data synthesis and discussion, *J. Struct. Geol.*, *14*, 1149–1156, doi:10.1016/0191-8141(92)90066-6.

Doake, C. S. M., H. F. J. Corr, A. Jenkins, K. Makinson, K. W. Nicholls, C. Nath, A. M. Smith, and D. G. Vaughan (2001), Rutford Ice Stream, Antarctica, in *The West Antarctic Ice Sheet: Behavior and Environment, Antarct. Res. Ser.,* vol. 77, edited by R. B. Alley and R. A. Bindschadler, pp. 221–235, AGU, Washington, D. C., doi:10.1029/AR077p0221

Dreger, D. S., and B. Woods (2002), Regional distance seismic moment tensors of nuclear explosions, *Tectonophysics*, *356*, 139–156, doi:10.1016/S0040-1951(02)00381-5.

Dreger, D. S., H. Tkalcic, and M. Johnston (2000), Dilational processes accompanying earthquakes in the long valley caldera, *Science*, *288*, 122–125.

Drew, J., R. S. White, F. Tilmann, and J. Tarasewicz (2013), Coalescence microseismic mapping, *Geophys. J. Int.*, *195*, 1773–1785, doi:10.1093/gji/ggt331.

Ekström, G., M. Nettles, and G. A. Abers (2003), Glacial earthquakes, *Science*, *302*, 622–624, doi:10.1126/science.1088057.

Engelhardt, H., N. Humphrey, B. Kamb, and M. Fahnestock (1990), Physical conditions at the base of a fast moving Antarctic ice stream, *Science*, *248*, 57–59, doi:10.1126/science.248.4951.57.

Gudmundsson, G. H. (2006), Fortnightly variations in the flow velocity of Rutford Ice Stream, West Antarctica, *Nature*, *444*, 1063–1064, doi:10.1038/nature05430.

Hanks, T. C., and H. Kanamori (1979), A moment magnitude scale, *J. Geophys. Res.*, *84*(9), 2348–2350, doi:10.1029/JB084iB05p02348.

Harland, S. R., J. M. Kendall, G. W. Stuart, G. E. Lloyd, A. F. Baird, A. M. Smith, H. D. Pritchard, and A. M. Brisbourne (2013), Deformation in Rutford Ice Stream, West Antarctica: Measuring shear-wave anisotropy from icequakes, *Ann. Glaciol.*, *54*, 105–114, doi:10.3189/2013AoG64A033.

King, E. C., R. C. A. Hindmarsh, and C. R. Stokes (2009), Formation of mega-scale glacial lineations observed beneath a West Antarctic ice stream, *Nat. Geosci.*, *2*, 585–588, doi:10.1038/NGEO581.

Kohnen, H. (1974), The temperature dependence of seismic waves in ice, *J. Glaciol.*, *13*, 144–147.

Lay, T., and T. C. Wallace (1995), *Modern Global Seismology*, vol. 58, 1st ed., chap. 9.4 Magnitude Scales, pp. 370–383, Acad. Press, London.

Lomax, A., J. Virieux, P. Volant, and C. Berge-thierry (2000), Probabilistic earthquake location in 3D and layered models: Introduction of a Metropolis-Gibbs method and comparison with linear locations, in *Advances in Seismic Event Location*, edited by C. H. Thurber and N. Rabinowitz, pp. 101–134, Kluwer, Amsterdam.

Murray, T., A. M. Smith, M. A. King, and G. P. Weedon (2007), Ice flow modulated by tides at up to annual periods at Rutford Ice Stream, West Antarctica, *Geophys. Res. Lett.*, *34*, L18503, doi:10.1029/2007GL031207.

Murray, T., H. Corr, A. Forieri, and A. M. Smith (2008), Contrasts in hydrology between regions of basal deformation and sliding beneath Rutford Ice Stream, West Antarctica, mapped using radar and seismic data, *Geophys. Res. Lett.*, *35*, L12504, doi:10.1029/2008GL033681.

Paterson, W. S. B. (1994), *The Physics of Glaciers*, 3rd ed., 480 pp., Pergamon, New York.

Peters, L. E., S. Anandakrishnan, R. B. Alley, and D. E. Voigt (2012), Seismic attenuation in glacial ice: A proxy for englacial temperature, *J. Geophys. Res.*, *117*, F02008, doi:10.1029/2011JF002201.

Pratt, M. J., J. P. Winberry, D. A. Wiens, S. Anandakrishnan, and R. B. Alley (2014), Seismic and geodetic evidence for grounding-line control of Whillans Ice Stream stick-slip events, *J. Geophys. Res. Earth Surf.*, *119*, 333–348, doi:10.1002/2013JF002842.

Reasenburg, P., and D. H. Oppenheimer (1985), FPFIT, FPPLOT and FPPAGE; Fortran computer programs for calculating and displaying earthquake fault-plane solutions, USGS Open-File Rep., pp. 85–739, U.S. Geological Survey, Denver, Colo.

Rignot, E., I. Velicogna, M. R. van den Broeke, A. Monaghan, and J. T. M. Lenaerts (2011), Acceleration of the contribution of the Greenland and Antarctic ice sheets to sea level rise, *Geophys. Res. Lett.*, *38*, L05503, doi:10.1029/2011GL046583.

Roethlisberger, H. (1972), Seismic exploration in cold regions, Tech. Monogr. 11-A 2a, Cold Regions Res. and Eng. Laboratory, U.S. Army Corps of Engineers, Hannover, N. H.

Smith, A. M. (1997a), Basal conditions on Rutford Ice Stream, West Antarctica, from seismic observations, *J. Geophys. Res.*, *102*, 543–552, doi:10.1029/96JB02933.

Smith, A. M. (1997b), Variations in basal conditions on Rutford Ice Stream, West Antarctica, *J. Glaciol.*, *43*, 245–255.

Smith, A. M. (2006), Microearthquakes and subglacial conditions, *Geophys. Res. Lett.*, *33*, L24501, doi:10.1029/2006GL028207.

Smith, A. M. (2007), Subglacial bed properties from normal-incidence seismic reflection data, *J. Environ. Eng. Geophys.*, *12*, 3–13, doi:10.2113/JEEG12.1.3.

Smith, A. M., and T. Murray (2009), Bedform topography and basal conditions beneath a fast-flowing West Antarctic ice stream, *Quat. Sci. Rev.*, *28*, 584–596, doi:10.1016/j.quascirev.2008.05.010.

Smith, A. M., T. Murray, K. W. Nicholls, K. Makinson, G. Aoalgeirsdóttir, A. E. Behar, and D. G. Vaughan (2007), Rapid erosion, drumlin formation, and changing hydrology beneath an Antarctic ice stream, *Geology*, *35*, 127–130, doi:10.1103/G23036A.

Thompson, J., M. Simons, and V. C. Tsai (2014), Modeling the elastic transmission of tidal stresses to great distances inland in channelized ice streams, *Cryosphere Discuss.*, *8*, 2119–2177, doi:10.5194/tcd-8-2119-2014.

Vaughan, D. G., A. M. Smith, P. C. Nath, and E. Le Meur (2003), Acoustic impedance and basal shear stress beneath four Antarctic ice streams, *Ann. Glaciol.*, *36*, 225–232, doi:10.3189/172756403781816437.

Wadati, K. (1933), On the travel time of earthquake waves, Part II, *Geophys. Mag.*, *7*, 101–111.

Waldhauser, F., and W. L. Ellsworth (2000), A double-difference earthquake location algorithm: Method And application to the Northern Hayward Fault, California, *Bull. Seismol. Soc. Am.*, *90*, 1353–1368, doi:10.1785/0120000006.

Walter, F., J. F. Clinton, N. Deichmann, D. S. Dreger, S. E. Minson, and M. Funk (2009), Moment tensor inversions of icequakes on Gornergletscher, Switzerland, *Bull. Seismol. Soc. Am.*, *99*, 852–870, doi:10.1785/0120080110.

Walter, F., D. S. Dreger, J. F. Clinton, N. Deichmann, and M. Funk (2010), Evidence for near-horizontal tensile faulting at the base of Gornergletscher, a Swiss Alpine glacier, *Bull. Seismol. Soc. Am.*, *100*, 458–472, doi:10.1785/0120090083.

Wiens, D. A., S. Anandakrishnan, J. P. Winberry, and M. A. King (2008), Simultaneous teleseismic and geodetic observations of the stick-slip motion of an Antarctic ice stream, *Nature*, *453*, 770–774, doi:10.1038/nature06990.

Winberry, J. P., S. Anandakrishnan, and R. B. Alley (2009), Seismic observations of transient subglacial water-flow beneath MacAyeal Ice Stream, West Antarctica, *Geophys. Res. Lett.*, *36*, L11502, doi:10.1029/2009GL037730.

Winberry, J. P., S. Anandakrishnan, D. A. Wiens, and R. B. Alley (2013), Nucleation and seismic tremor associated with the glacial earthquakes of Whillans Ice Stream, Antarctica, *Geophys. Res. Lett.*, *40*, 312–315, doi:10.1002/grl.50130.

Zhu, L., and L. A. Rivera (2002), A note on the dynamic and static displacements from a point source in multilayered media, *Geophys. J. Int.*, *148*, 619–627, doi:10.1046/j.1365-246X.2002.01610.x.